Supporting Information for "The GFDL Global Atmosphere and Land Model AM4.0/LM4.0 – Part II: Model Description, Sensitivity Studies, and Tuning"

M. Zhao[1], J.-C. Golaz[1,5], I. M. Held[1], H. Guo[2], V. Balaji[3], R. Benson[1], J.-H. Chen[1], X. Chen[3], L. J. Donner[1], J. P. Dunne[1], K. Dunne[4], J.Durachta[1], S.-M. Fan[1], S. M. Freidenreich[1], S. T. Garner[1], P. Ginoux[1], L. M. Harris[1], L. W. Horowitz[1], J. P. Krasting[1], A. R. Langenhorst[1,8], Z. Liang[1], P. Lin[1], S.-J. Lin[1], S. L. Malyshev[1], E. Mason[6], P. C. D. Milly[1,4], Y. Ming[1], V. Naik[1], F. Paulot[3], D. Paynter[1], P. Phillipps[1], A Radhakrishnan[6], V. Ramaswamy[1], T. Robinson[6], D. Schwarzkopf[1], C. J. Seman[1], E. Shevliakova[1], Z. Shen[3], H. Shin[3], L. G. Silvers[3], J. R. Wilson[7], M. Winton[1], A. T. Wittenberg[1], B. Wyman[1], and B. Xiang[2]

[1]GFDL/NOAA, Princeton, New Jersey, USA
[2]UCAR/GFDL, Princeton, New Jersey
[3]Princeton University/GFDL, Princeton, New Jersey
[4]U.S. Geological Survey, Princeton, New Jersey
[5]Lawrence Livermore National Laboratory, Livermore, California
[6]Engility Corporation/GFDL, New Jersey
[7]NASA Ames Research Center, Moffett Field, California
[8]Deceased

Corresponding author: Ming Zhao, Ming.Zhao@noaa.gov

S1 Treatment of energy conservation in dynamical core

The dissipation of kinetic energy in this model, besides the part due to explicit vertical diffusion, occurs implicitly as a consequence of the advection algorithm. As a result, the dissipative heating balancing this loss of kinetic energy cannot easily be computed locally, and is, instead returned to the flow by a spatially uniform tropospheric heating. This dissipative heating associated with the advection in the dynamical core in AM4.0 is $\sim 2\ \mathrm{W\,m^{-2}}$.

There is also another energy conservation inconsistency in that the energy conserved by the dynamical core involves a potential energy computed with the virtual temperature, while the model column physics uses temperature without the virtual effect, assuming that the conservation of internal plus potential energy, vertically integrated, reduces to the conservation of vertically integrated enthalpy, c_pT. This discrepancy averages to $0.4\ \mathrm{W\,m^{-2}}$. We adjust the dissipative heating correction in the dynamical core to account for this discrepancy. As a result, there is good consistency, within $0.1\ \mathrm{W\,m^{-2}}$, between energy fluxes at the TOA and at the surface in equilibrium, with the net downward heat surface flux defined as $R_{sfc} - L_vE - S - L_fP_{snow}$. Here R_{sfc} is net downward LW + SW radiative flux, E surface evaporation of vapor, S upward sensible heat flux, P_{snow} surface precipitation flux of frozen water, L_v and L_f are the latent heat of vaporization and fusion respectively. A remaining problem is that these latent heats are assumed to be independent of temperature. Removing the latter inaccuracy in the most appropriate fashion would involve multiple changes to the code and was postponed to another development cycle.

S2 A tabular list of radiation change between AM3 and AM4.0

Table S1. Description of radiation change between AM3 and AM4.0.

Component	AM3	AM4.0
Longwave		
H_2O Line Database Continuum	HITRAN 2000 CKD2.1	HITRAN 2012 MT CKD 2.5
CO_2 Line Database Amounts Spectral Range	HITRAN 2000 1-1600 ppmv 500-850 $\mathrm{cm^{-1}}$	HITRAN 2012 1-10000 ppmv 500-850, 990-1200 $\mathrm{cm^{-1}}$
N_2O Line Database Amounts	HITRAN 2000 0-500 ppbv	HITRAN 2012 0-800 ppbv
CH_4 Line Database Amounts	HITRAN 2000 0-4000 ppbv	HITRAN 2012 0-6000 ppbv
Shortwave		
H_2O Line Database Absorbing Region Continuum	HITRAN 2000 Troposphere only CKD2.1 foreign only	HITRAN 2012 Troposphere + Stratosphere BPS 1.1 Foreigh; BPS 2.0 Self
O_2 Line Database Continuum	HITRAN 2000 None	HITRAN 2012 HITRAN CIA
N_2 Line Database	None	HITRAN CIA
CO_2 Line Database	HITRAN 2000	HITRAN 2012
CH_4 Line Database	None	HITRAN 2012

S3 Treatment of convective precipitation and its reevaporation

At any given level, the updraft condensate $q_{c,u}$ in a shallow or deep plume is partitioned into liquid ($q_{l,u} = f_l q_{c,u}$) and ice phase [$q_{i,u} = (1 - f_l)q_{c,u}$] based on the updraft temperature (T):

$$f_l(T) = \begin{cases} 1 & , T > 268\text{K} \\ 1 - \frac{268-T}{20} & , 248 \leq T \leq 268\text{K} \\ 0 & , T < 248\text{K} \end{cases} \tag{S1}$$

As a plume rises, part of the updraft liquid and ice water is removed as precipitation following:

$$\begin{aligned} P_l &= e_l \delta p \; max(q_{l,u} - q_{l0}, 0) \\ P_i &= e_i \delta p \; q_{i,u} \end{aligned} \tag{S2}$$

where e_l and e_i denote respectively a specified efficiency in converting liquid and ice water into rain and snow. q_{l0} denotes a threshold liquid water content below which no liquid precipitation is allowed. δp represents the depth of a vertical layer of the model so that e_l, e_i have units of Pa^{-1}. In addition, $e_l \delta p$, and $e_i \delta p$ are capped at 1. e_l, e_i, and q_{l0} are tunable parameters; in AM4.0 they are set respectively to be 6E-5 Pa^{-1}, 11E-5Pa^{-1}, and 0.2 $\text{g}\,\text{kg}^{-1}$.

At each level, the convective precipitation flux has contributions from both the detrained precipitating condensate P_l and P_i from the level in question and from the condensate falling from above. For both shallow and deep plumes, precipitating condensate is allowed to evaporate (or sublimate) as it falls through a sub-saturated environment very similar to that used in the relaxed Arakawa-Schubert scheme in AM2 [*GFDL-GAMDT*, 2004; *Moorthi and Suarez*, 1999]. Since the details of the precipitation re-evaporation scheme is not documented in the AM2 paper [*GFDL-GAMDT*, 2004], we provide a description of this scheme below.

As the condensate falls through a sub-saturated layer with ambient temperature T and relative humidity H, the amount of precipitating water being evaporated over a model's physics time step Δt is formulated as:

$$E_p = \frac{q_s(T)\max(H_c - H, 0)}{1 + H_c \frac{L}{c_p}\frac{dq_s}{dT}} f(\alpha P) \tag{S3}$$

where q_s is saturation specific humidity, L the latent heat of evaporation (or sublimation), and c_p the heat capacity. H_c is a critical value of relative humidity below which precipitation is allowed to evaporate that roughly accounts for the fact that convective precipitation only moistens a portion of a grid-box and may not necessarily bring the grid-box towards saturation. $f(\alpha P)$ represents evaporation efficiency which is a function of total precipitation flux P at a layer and an assumed fraction (α) of P falling outside the saturated region. $f(\alpha P)$ is parameterized following *Sud and Molod* [1988] as:

$$f(\alpha P) = 1 - e^{c_1 \Delta t (c_2 \sqrt{\sigma} \alpha P)^{\frac{1}{2}}} \tag{S4}$$

where c_1=$-0.000544\ \text{s}^{-1}$, c_2=$194.4\ \text{kg}^{-1}\,\text{m}^2\text{s}$, $\sigma = p/p_s$ with p and p_s denoting the pressure at current layer and surface respectively. P is in unit of $\text{kg}\,\text{m}^{-2}\text{s}^{-1}$. At any given layer, the evaporated water E_p is compared to precipitation to ensure it does not exceed the available precipitating water at that layer. E_p is used to compute the cooling and moistening tendencies due to evaporation of precipitation, which are subsequently added to the total convective tendencies.

Both α and H_c are tunable parameters, which can be used to control the strength of precipitation re-evaporation in this convection scheme. We use the same values of H_c

and α for both shallow and deep plumes. In AM4.0, α is set to be 0.15. To enhance the rain evaporation and the cold pool effect in the PBL, we use a larger H_c (95%) in the PBL than that (85%) in the free troposphere.

S4 Treatment of convective gustiness

In the double plume convection scheme, we also include a prognostic representation of convective gustiness G_c with a source term driven by the PBL vertically integrated negative buoyancy due to precipitation re-evaporation and a sink term that relaxes G_c towards zero.

$$\frac{\partial G_c}{\partial t} = -\int_{z_s}^{z_{PBL}} \frac{1}{T}\left(\frac{\partial T}{\partial t}\right)_{evap} g dz - \frac{G_c}{\tau_g} \tag{S5}$$

where z_{PBL} denotes PBL height, *evap* denotes the tendencies due to evaporation of convective precipitation. The relaxation time scale τ_g in AM4.0 is set to 2 hours roughly consistent with that derived from the cloud resolving model (CRM) studies [e.g., *Tompkins*, 2001]. In the current implementation, G_c is used only over the land regions where the cloud-base vertical velocity derived from the boundary layer turbulent kinetic energy (TKE) and convective inhibition (CIN) [see Eq. 28 in *Bretherton et al.*, 2004] is zero (i.e., when CIN is so large that PBL TKE is not strong enough to break it; this occurrs usually at night). This convective gustiness is not currently used in the surface flux calculation. In AM4.0 if G_c exceeds a tunable threshold parameter G_{c0} ($2\mathrm{m}^2\mathrm{s}^{-2}$) and CAPE is larger than CIN, a forced lifting is performed to help initiate the deep plume [i.e., negative vertical velocity below the level of free convection (LFC) is simply replaced with a small positive value, $1\ \mathrm{m\,s^{-1}}$], so that the plume can still arrive at its LFC. Since CIN is weak over the oceans, we decided to apply this convective gustiness scheme only over land. While this is a crude way for representing the forced convection over land, we find this implementation helps to reduce a dry bias over the Amazon. Because Amazon rainfall is consistently biased low in coupled simulations, and this dry bias can be very significant in models with interactive vegetation and land carbon cycle, we have opted to include this scheme here despite its arbitrariness. While we were hopeful that this addition to the convection scheme would improve the overall bias in the diurnal cycle of precipitation over land as described in *Zhao et al.* [2018], it has no significant effect on that bias.

S5 Sensitivity to convection parameterization

S5.1 A tabular list of TOA radiative fluxes from perturbed convection runs

Table S2: Global TOA radiative fluxes (unit: $\mathrm{W\,m^{-2}}$) from AM4.0 simulations with varying convection parameters. See the main text for a description of the experiments.

S5.2 Wavenumber-frequency power spectrum from the perturbed ε_1 runs

Fig. S1: Normalized tropical (15°S-15°N) symmetric OLR wavenumber-frequency power spectrum as in Fig. 27d of *Zhao et al.* [2018] except for (a) C1, (b) C2, (c) C3, (d) C4. See main text for a description of the experiments. Colored shading shows power associated with MJO, Kelvin, and other tropical convective waves that are significantly above an approximately red-noise background power spectra. The colored lines represent various equatorial wave dispersion curves labeled for five different equivalent depths (8, 12, 25, 50, and 90m).

Table S2. Global TOA radiative fluxes (unit: $\mathrm{W\,m^{-2}}$) from AM4.0 simulations with varying convection parameters. See main text for a description of the experiments. OLR: TOA outgoing LW radiation, SWABS: TOA net downward SW radiation, NETRAD: TOA net radiation (positive: downward). LW, SW, and total CREs are respectively for the LW, SW and total cloud radiative effects

Exp	OLR	SWABS	NETRAD	LW CRE	SW CRE	total CRE
C0	238.54	240.23	1.69	23.68	-48.54	-24.86
C1	237.76	241.67	3.92	24.17	-47.16	-22.98
C2	237.92	240.66	2.74	24.09	-48.15	-24.05
C3	239.30	240.25	0.95	23.12	-48.49	-25.37
C4	239.96	240.38	0.42	22.61	-48.35	-25.74
C5	239.43	243.41	3.97	23.16	-45.04	-21.88
C6	238.53	241.21	2.68	23.80	-47.52	-23.72
C7	238.54	239.74	1.19	23.64	-49.08	-25.44
C8	238.47	239.42	0.95	23.68	-49.45	-25.77
C9	238.69	241.37	2.68	23.54	-47.40	-23.87

S5.3 AM4.0 sensitivity to convective precipitation re-evaporation

The strength of the precipitation re-evaporation also affects the climate simulation significantly. To demonstrate this, we modified the parameter α (see Eq. S3-S4) that controls the fraction of precipitation falling outside of the convective updrafts, from the AM4.0 default value 0.15 to 0 (turning off convective precipitation re-evaporation), 0.05, 0.25, 0.35 and refer to the 4 models as C5, C6, C7 and C8 respectively. Fig. S2 shows the simulated difference in precipitation between each perturbation experiment and the control experiment. As α decreases, there is also a reduction of precipitation in the Philippine Sea and increase of precipitation over the Maritime continent and equatorial Indian ocean broadly similar to the decreasing ε_1 experiments described in the text. In addition, there is a substantial increase in precipitation over the eastern Pacific ITCZ, especially over the eastern Pacific warm pool. The shift of precipitation from the west to east in the Pacific (resulting in a precipitation simulation similar to that of HiRAM) helps to produce more eastern and less western Pacific TCs, which is desirable for optimization of TC climatology (and a desirable feature of the HiRAM AMIP simulations of TCs). However, early experiments with coupled versions of this model indicated that the strengthening of the eastern Pacific ITCZ tends to produce a larger equatorial cold SST bias. In determining the AM4.0, we consider the coupled simulation as a high priority and therefore did not focus on the optimizations of eastern Pacific TCs or the reduction of western Pacific precipitation.

Similar to the varying ε_1 experiments, the fraction of large-scale precipitation decreases with decreasing α due presumably to the enhanced convective precipitation efficiency. This sensitivity is however significantly lower than that from ε_1; for example, the tropical mean f_l is reduced by roughly 15% (20%) in C5 (C1) from its control value in C0.

Despite the broad similarity in precipitation sensitivity to decreasing ε_1 and decreasing α, AM4.0 shows very different response in upper tropospheric temperature to the two parameter changes. Fig. S3 shows that as α decrease, there is a significant cooling in the upper tropospheric temperature despite an increase of tropical mean convec-

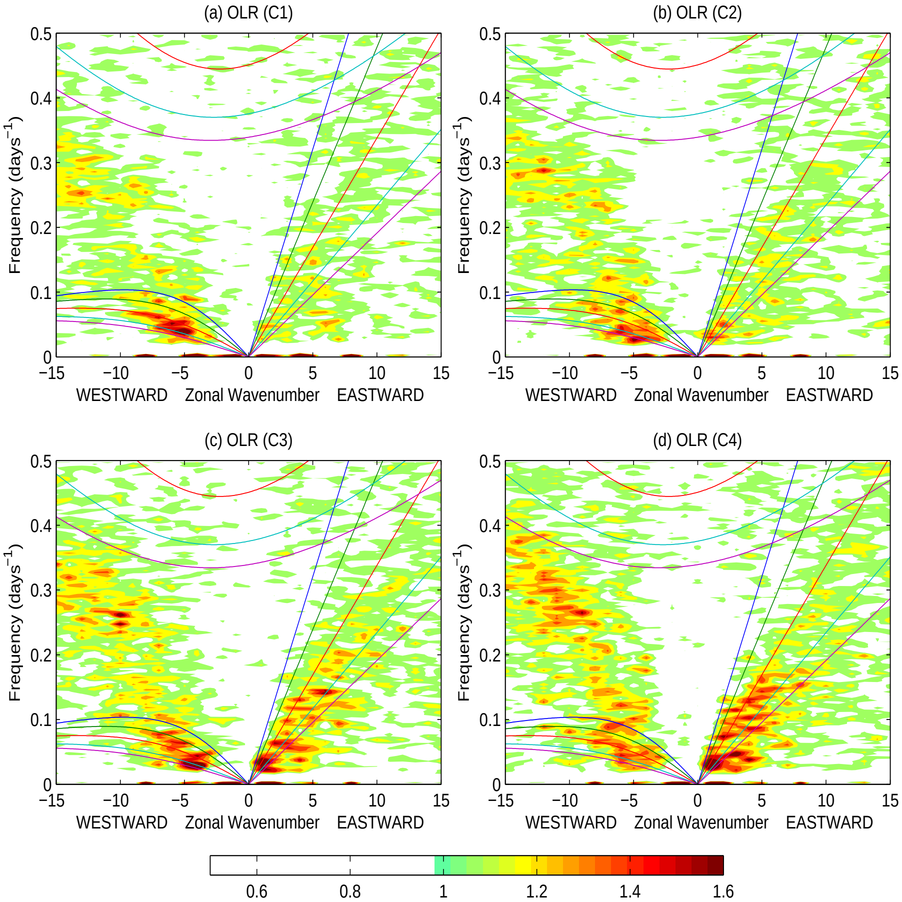

Figure S1. Normalized tropical (15°S-15°N) symmetric OLR wavenumber-frequency power spectrum as in Fig. 27d of *Zhao et al.* [2018] except for (a) C1, (b) C2, (c) C3, (d) C4. See main text for a description of the experiments. Colored shading shows power associated with MJO, Kelvin, and other tropical convective waves that are significantly above an approximately red-noise background power spectra. The colored lines represent various equatorial wave dispersion curves labeled for five different equivalent depths (8, 12, 25, 50, and 90m).

tive precipitation. This suggests that the upper tropospheric temperature is not simply determined by the total amount of convective precipitation. It is rather likely determined by the temperature in the deep convective plumes. Different from a reduction of ε_1, a decrease in α does not directly modify the deep plume temperature. Instead, it produces more drying and warming in the lower atmosphere so that subsequent plumes are affected through entrainment. As the deep plumes penetrate through the drier environment, its temperature becomes colder, with the same amount of lateral mixing, because more plume condensate is evaporated. This environmental feedback can lead to a decrease of plume temperature in upper troposphere. In AM4.0, a drier and warmer low troposphere can lead to an enhancement of plume lateral mixing, which would further increase this feedback.

Finally, it is worth noting that α can also affect AM4.0 simulations of the tropical transients. In particular, the model simulated MJO and Kelvin waves tend to be stronger with an increase of α although this sensitivity is not as large as that from the varying ε_1 experiments (see Fig. S4). The interactions among the parameterized convection, the

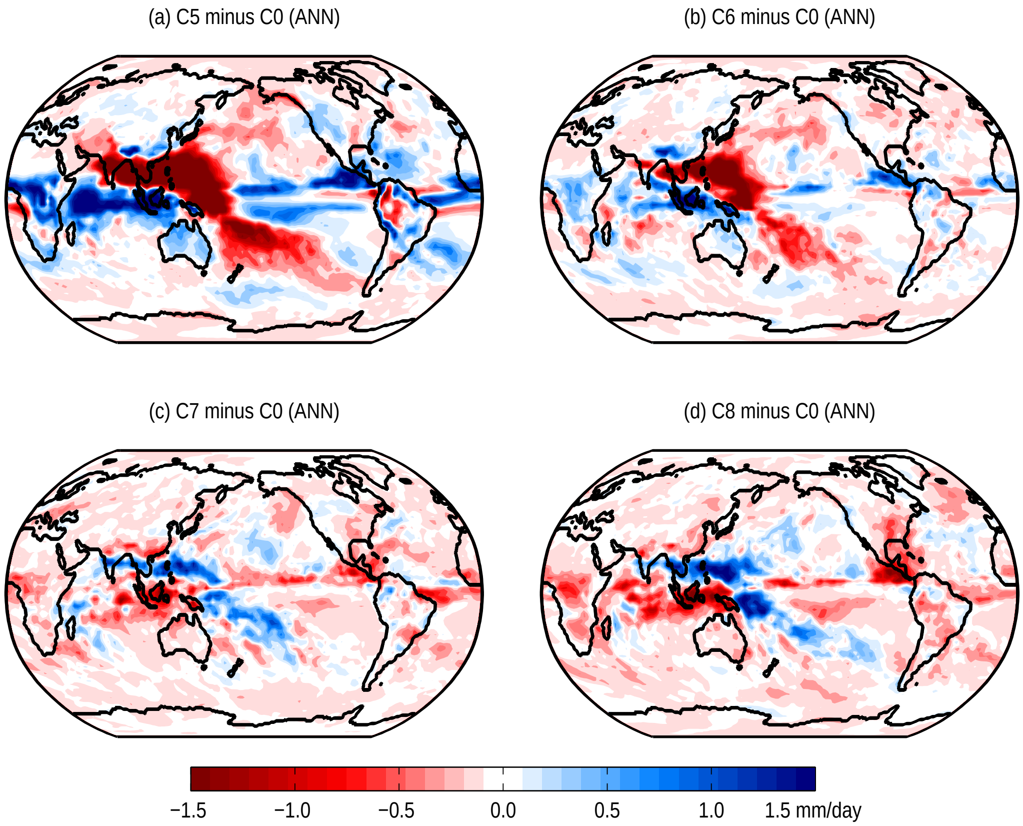

Figure S2. Geographical distribution of the difference in long-term annual mean surface precipitation for (a) C5 minus C0, (b) C6 minus C0, (c) C7 minus C0, and (d) C8 minus C0. See text for a description of the experiments.

PBL, the CRE, and the large-scale dynamics are presumably important to this sensitivity. We will leave a detailed study of the mechanisms responsible for this sensitivity and the sensitivity to ε_1 for a future paper.

S5.4 AM4.0 sensitivity to EIS constraint

Fig. S5: Changes in low cloud amount between P2K (uniform 2K increase of SSTs) and the control experiments for (a) C0, (b) C9, and (c) their difference: (a) minus (b).

Fig. S6: As in Fig. 8 except for changes between P2K and the corresponding control simulation.

S6 Sensitivity to orographic drag parameterization

Fig. S7: Model bias in winter time (DJF) 850 hPa zonal wind compared to ERA-Interim for (a) C0 and (b) C0-SP88. (c) shows the difference between (a) and (b).

Fig. S8: (a) The change of zonal mean zonal wind wind with increase of propagating drag coefficient by 30% from 0.9 to 1.17. (b) is similar to (a) but for the increase of blocking drag coefficient by 30% from 3.0 to 3.9.

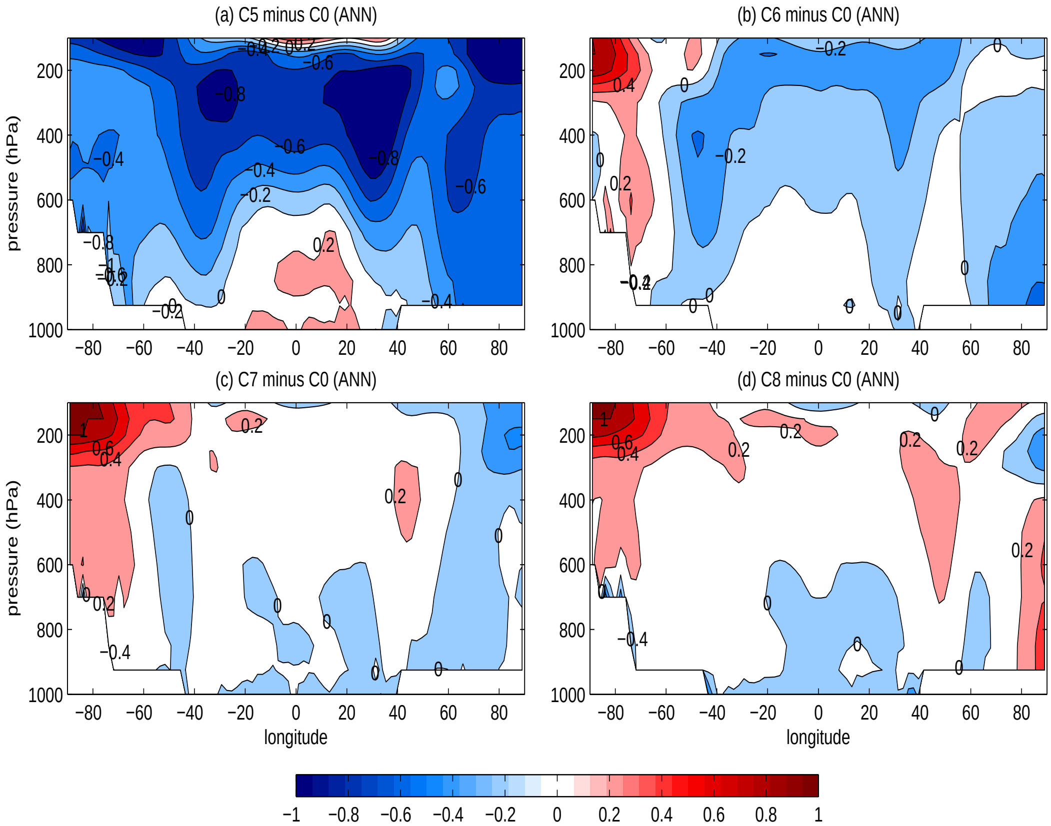

Figure S3. Annual and zonal mean tropospheric temperature difference (unit: K) for (a) C5 minus C0, (b) C6 minus C0, (c) C7 minus C0, and (d) C8 minus C0.

A number of experiments have been conducted to uncover the sensitivity to the main parameters of the G05 scheme. One of these is to increase the blocking drag coefficient a_b from 3.0 to 3.9, and another is to increase the propagating drag coefficient a_p proportionally from 0.9 to 1.17. During boreal winter (DJF), the surface air temperature response is similar for the two cases, namely an increased cold bias in the Arctic with increasing drag (not shown). The circulation changes at 850 hPa are shown in Fig. S9. The response to the propagating drag coefficient is stronger than to a_b. With increased a_p, the 850 hPa zonal wind simulation is generally improved. However, this comes at the expense of the stratospheric winds, which are degraded. The tropospheric response consists primarily of a southward shift of the subtropical jet in the Northern Hemisphere. Counter-intuitively, the stratospheric zonal wind shows an increase in the positive bias.

References

Bretherton, C. S., J. R. McCaa, and H. Grenier (2004), A new parameterization for shallow cumulus convection and its application to marine subtropical cloud-topped boundary layers. Part I: Description and 1-d results, *Mon. Wea. Rev.*, *132*, 864–882.

GFDL-GAMDT (2004), The new GFDL global atmosphere and land model AM2/LM2: Evaluation with prescribed SST simulations, *J. Climate*, *17*, 4641–4673.

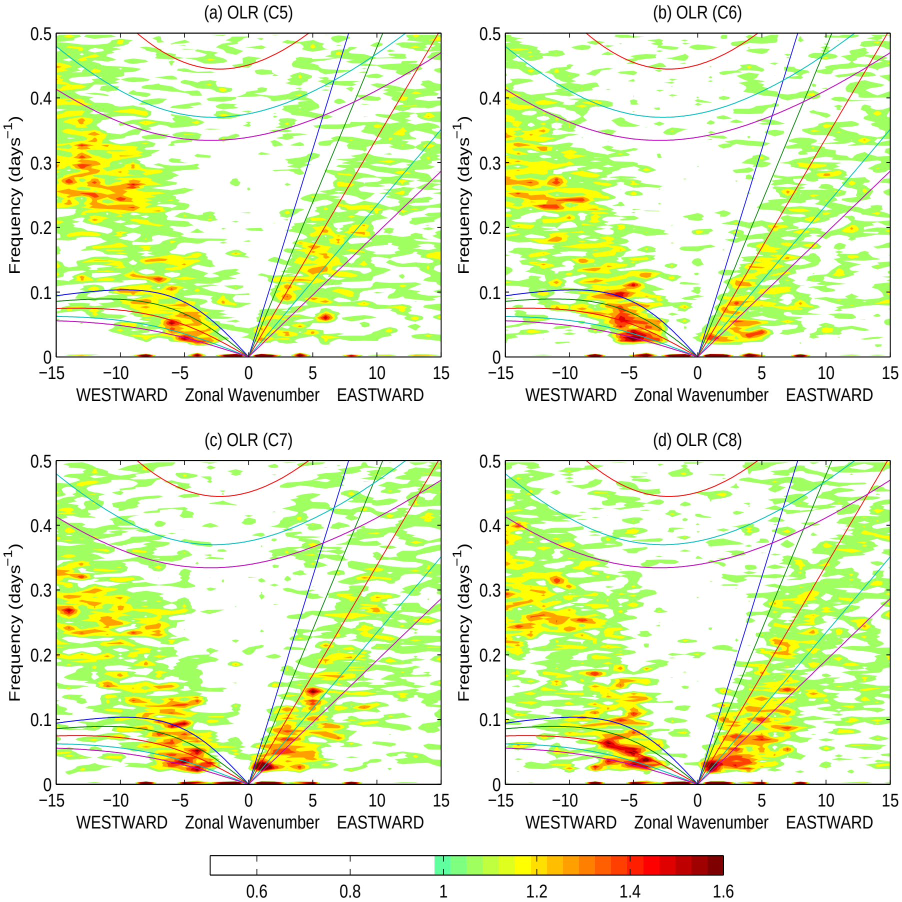

Figure S4. As in Fig. S1 except for C5-C8 perturbation experiments.

Moorthi, S., and M. Suarez (1999), Documentation of version 2 of Relaxed Arakawa-Schubert cumulus parameterization with convective downdrafts, *NOAA Tech. Rep*, pp. 44, NWS/NCEP 99–01, Camp Springs, MD.

Sud, Y., and A. Molod (1988), The roles of dry convection, cloud-radiation feedback processes and the influence of recent improvements in the parameterization of convection in the GLA GCM, *Mon. Wea. Rev.*, *116*, 2366–2387.

Tompkins, A. M. (2001), Organization of tropical convection in low vertical wind shears: the role of cold pools, *J. Atmos. Sci.*, *58*, 1650 1672.

Zhao, M., J.-C. Golaz, I.M. Held, H. Guo, and 41 co-authors (2018), The GFDL global atmosphere and land model AM4.0/LM4.0 – Part I: Simulation Characteristics with Prescribed SSTs, *J. of Adv. Model. Earth Syst., accepted with revision.*

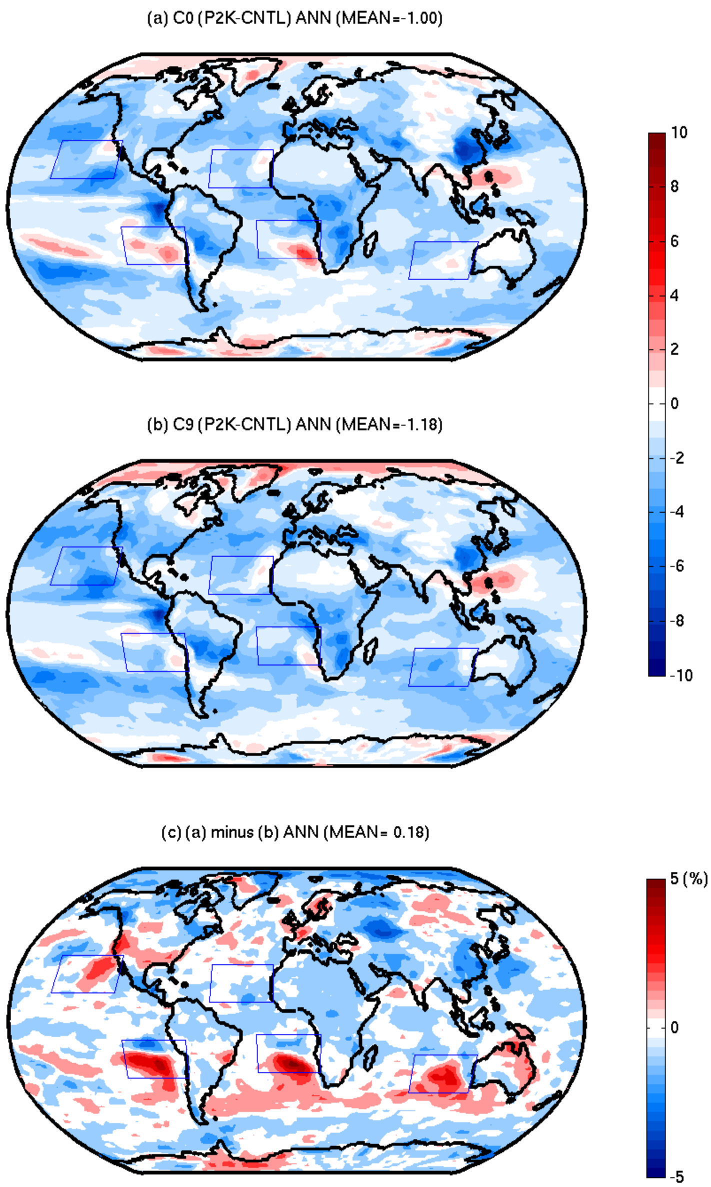

Figure S5. Changes in low cloud amount between P2K (uniform 2K increase of SSTs) and the control experiments for (a) C0, (b) C9, and (c) their difference: (a) minus (b).

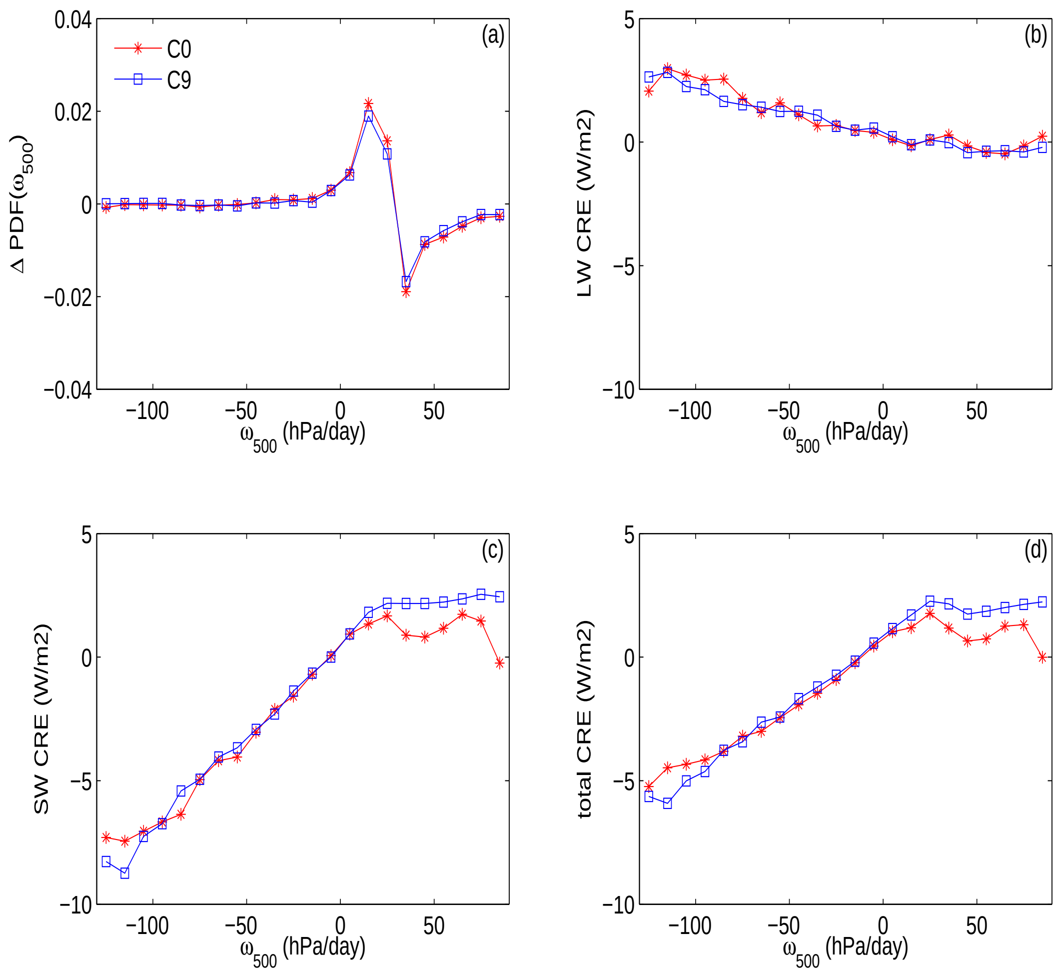

Figure S6. As in Fig. 8 except for changes between P2K and the corresponding control simulation.

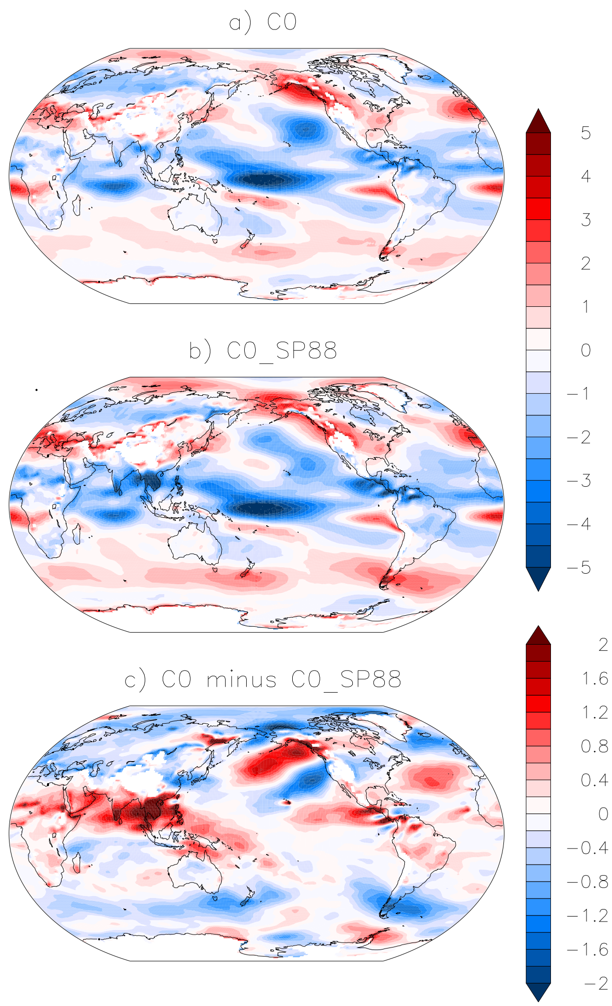

Figure S7. Model bias in winter time (DJF) 850 hPa zonal wind compared to ERA-Interim for (a) C0 and (b) C0-SP88. (c) shows the difference between (a) and (b).

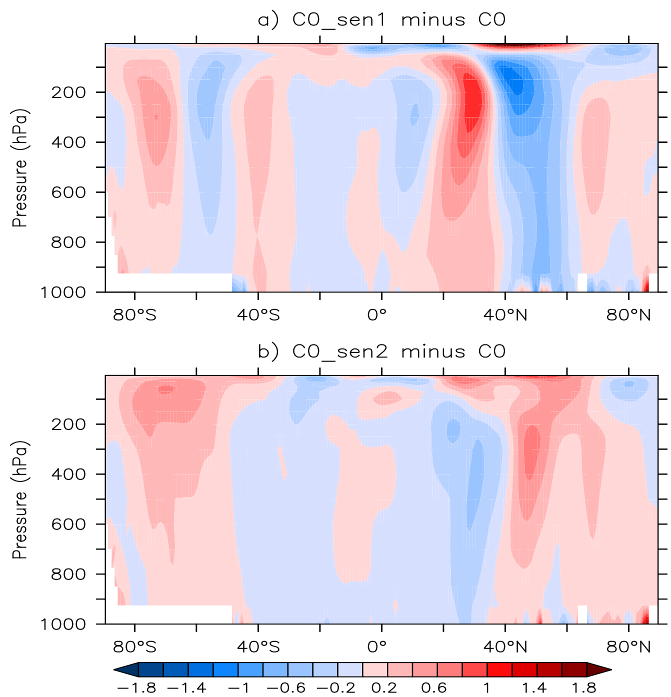

Figure S8. (a) The change of zonal mean zonal wind wind with increase of propagating drag coefficient by 30% from 0.9 to 1.17. (b) is similar to (a) but for the increase of blocking drag coefficient by 30% from 3.0 to 3.9.

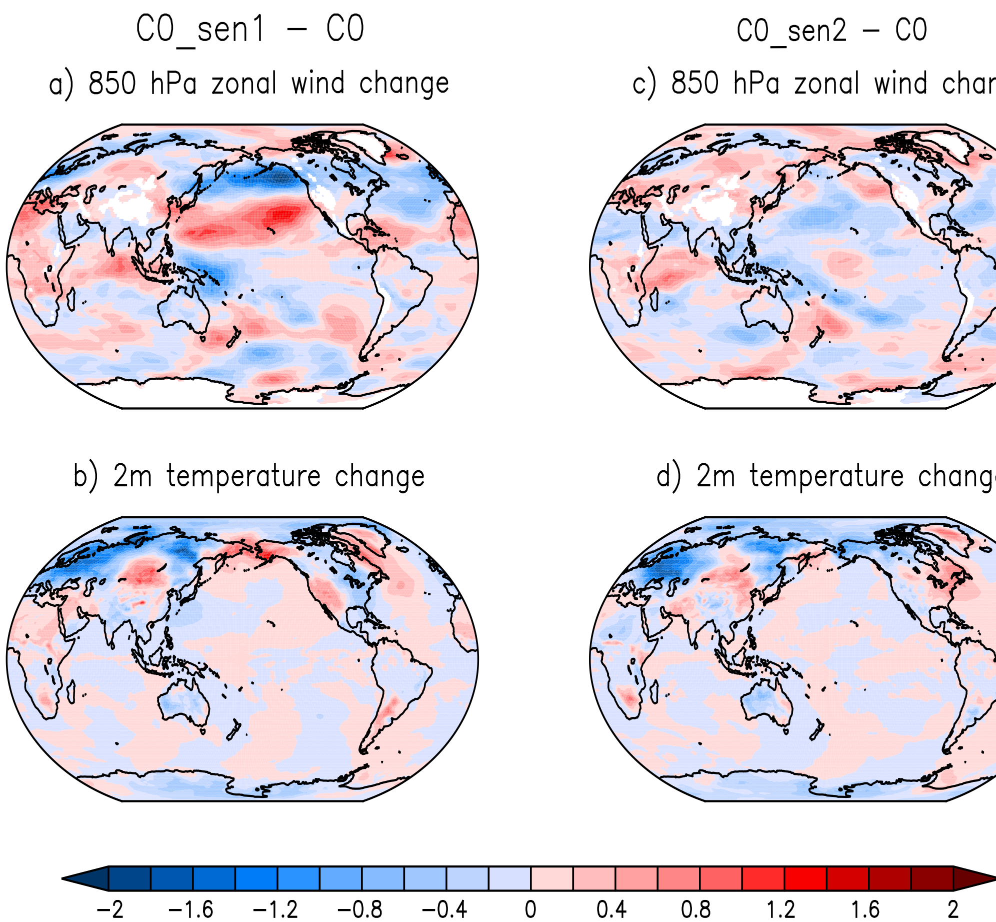

Figure S9. The changes of a) zonal wind at 850 hPa and b) 2m temperature with increase of propagating drag coefficient by 30% from 0.9 to 1.17. c-d) are similar to a-b) but for the increase of blocking drag coefficient by 30% from 3.0 to 3.9.